Hole transport theory in pseudomorphic $Si_{1-x}Ge_x$ alloys grown on Si(001) substrates

J. M. Hinckley and J. Singh
Center for High Frequency Microelectronics, Department of Electrical Engineering and Computer Science, The University of Michigan, Ann Arbor, Michigan 48109-2122
(Received 19 May 1989)

The physics of hole transport in pseudomorphic $Si_{1-x}Ge_x$/Si(001) is investigated by Monte Carlo simulation. The Monte Carlo method developed in this work takes into account several aspects of the strained *p*-type system which qualitatively distinguish it from an *n*-type system. (1) The valence-band system is described with use of a three-band $\mathbf{k}\cdot\mathbf{p}$ method which gives an accurate representation of the strongly coupled heavy-hole, light-hole, and split-off–hole states. (2) The valence-band deformation-potential theory is used to determine both the strain effects on the band structure and the hole-phonon scattering rates in both strained and unstrained materials. (3) The scattering rates are anisotropic, depending upon the direction of flight and are calculated on a mesh which exploits the symmetry of the system. (4) The postscattering states are determined from a probability distribution which depends not only on the scattering angle, but also upon the initial direction of flight. The Monte Carlo method is used to make a detailed study of the effect of strain and alloying on hole transport in lightly doped pseudomorphic $Si_{1-x}Ge_x$ ($0 \le x \le 0.4$) grown on (001) Si, subjected to electric fields in the range of 1–20 kV/cm, at 300 K. The scattering mechanisms considered are: alloy scattering, acoustic-phonon scattering, and both Si-Si and Ge-Ge optical-phonon scattering. Each of these mechanisms can drive both intraband and interband scattering within and between all of the top three valence bands. The combined effects of strain and alloying are found to produce a monotonic increase in hole mobility and temperature, which at the highest Ge content alloy studied, $Si_{0.6}Ge_{0.4}$/Si(001), are comparable to the hole mobility and temperature in bulk Ge. A slightly greater carrier velocity is found for in-plane transport than for perpendicular transport.

I. INTRODUCTION

The effect of hydrostatic and uniaxial strain on the electronic band structure of semiconductors has been an area of active study for several decades. The information yielded by these studies is valuable in developing a better theoretical understanding of both the band structure as well as deformation-potential scattering of electrons and holes due to phonons. However, until comparatively recently, there has been little interest in studying charge-carrier transport in the presence of strain. This was because strain had to be introduced by some external apparatus such as a high-pressure diamond-anvil cell. This rendered the phenomena difficult to study, with the issue remaining of little technological importance.

The development of lattice-mismatched heteroepitaxy has resulted in an increase in the study of charge-carrier transport in strained semiconductors. Theoretical and experimental studies show that if a material with a bulk lattice constant a_L is grown as a film on a comparatively thick substrate with a different lattice constant a_S, the film will grow epitaxially, with an in-plane lattice constant of a_S and an adjustment, via the Poisson effect, in the perpendicular lattice constant. This pseudomorphic growth continues up to a critical thickness determined by a balance between strain and chemical energy. Beyond this thickness the overlayer relaxes, producing dislocations. The in-plane lattice constant of the film reverts to its bulk value a_L. For film thicknesses less than the critical thickness, a large strain can be produced in the film, which can greatly change its band structure, both by changing effective masses and lifting degeneracies. Since the pseudomorphic layer is thermodynamically stable, it is possible to fabricate semiconductor devices with strained layer components. The strain-induced band-structure changes may lead to increased charged carrier mobility within the pseudomorphic layers. This, in turn, becomes a useful way to increase the speed of semiconductor device operation.

The heteroepitaxial system of $Si_{1-x}Ge_x$ layers grown on Si substrates is of great technological interest for fabricating semiconductor devices. On the one hand, $Si_{1-x}Ge_x$ ($x > 0$) has a larger bulk lattice constant than Si and thus forms an epitaxial strained layer when grown on Si. This may lead to an increase of charge-carrier mobility, over that of Si. On the other hand, the $Si_{1-x}Ge_x$ material system offers an advantage over III-V compound semiconductors of being processable with existing, high-yield silicon processing methods. Although only comparatively recently studied as a strained heteroepitaxial material, it may reasonably be expected that $Si_{1-x}Ge_x$/Si heterostructure devices will form the backbone of very-large-scale–integrated (VLSI) circuits in the relatively near future. Optimum semiconductor device design is ultimately based upon a complete understanding and accurate modeling of charge-carrier transport. In this con-

text, hole (p-type) transport, which often limits the performance of complementary logic circuits, is particularly important to understand.

This paper presents the results of a Monte Carlo calculation of high-field hole transport in intrinsic $Si_{1-x}Ge_x$ lattice matched to (001) Si at $T=300$ K. The valence-band structure is calculated for the heavy-hole, light-hole, and split-off–hole bands by solving for the eigenvalues of the Shockley $\mathbf{k}\cdot\mathbf{p}$ matrix, in which spin-orbit coupling has been included. The hole-scattering mechanisms considered in this work are deformation-potential acoustical-phonon scattering, deformation-potential optical-phonon scattering, and random-alloy disorder scattering. These mechanisms are responsible for both intraband and interband transitions. Acoustic-phonon and alloy scattering are treated as being elastic, while optical-phonon emission and absorption are treated as distinct inelastic scattering processes. The optical-phonon spectrum is modeled as having a two-phonon mode behavior, with the presence of Si-like and Ge-like optical phonons. The strength of each is taken to be proportional to the mole fraction of each respective alloy constituent. Other scattering mechanisms are not considered in this work. Most notably, ionized impurity and carrier-carrier scattering are omitted. The effect of strain is introduced through the use of the valence-band deformation-potential theory.

The outline of the remainder of this paper is as follows. In Sec. II the theory behind our band structure and scattering rate calculations is described. Some of the aspects which make the hole band structure and scattering rates more complicated than in the case of electrons, are discussed. In Sec. III the features of our Monte Carlo implementation specifically pertaining to hole transport are presented. These include strong coupling effects in the band structure, interband scattering as well as intraband scattering, use of bidimensional postscattering state probability distributions, and anisotropic scattering rates. In Sec. IV the transport simulation results are given. These include a discussion of the effect of choice of alloy scattering potential, which, to date, is not well determined for the strained $Si_{1-x}Ge_x$ system. Also presented here are the calculated velocity-electric field and carrier temperature-electric field characteristics and mean collision times, as a function of ally composition, from 0 to 40 % Ge. Concluding remarks are made in Sec. V.

II. BAND STRUCTURE AND SCATTERING PROCESSES

The valence band structure used in this work is calculated using a three valence band $\mathbf{k}\cdot\mathbf{p}$ method. The eigenstates are composed from the six-dimensional basis $|x\uparrow\rangle$, $|y\uparrow\rangle$, $|z\uparrow\rangle$, $|x\downarrow\rangle$, $|y\downarrow\rangle$, $|z\downarrow\rangle$, where x,y,z, denote the three orbitals associated with the Γ'_{25} representation of the top of the valence band and $\uparrow$ and $\downarrow$ denote spin up ($+z$) and spin down ($-z$), respectively. A valence-band Hamiltonian matrix in this basis which was reported by Dresselhaus, Kip and Kittel[1] is

$$\underline{H}_{\mathbf{k}\cdot\mathbf{p}}=\begin{bmatrix}\underline{H}' & \underline{0}_{3\times3}\\ \underline{0}_{3\times3} & \underline{H}'\end{bmatrix}\begin{matrix}x,y,z\uparrow\\ x,y,z\downarrow\end{matrix},$$

$$\underline{H}'=\begin{bmatrix}Lk_x^2+M(k_y^2+k_z^2) & Nk_xk_y & Nk_zk_x\\ Nk_xk_y & Lk_y^2+M(k_z^2+k_x^2) & Nk_yk_z\\ Nk_zk_x & Nk_yk_z & Lk_z^2+M(k_x^2+k_y^2)\end{bmatrix}\begin{matrix}x\\ y\\ z\end{matrix}. \quad (1)$$

The effect of the conduction band and all higher bands is contained in the terms L, M, and N.

The wave-vector-independent spin-orbit interaction perturbation matrix is added to $\underline{H}_{\mathbf{k}\cdot\mathbf{p}}$ to obtain the Hamiltonian matrix for the valence band of an unstrained material. In the above basis, the spin-orbit perturbation matrix is[2]

$$\underline{H}_{\text{s.o.}}=\frac{\Delta_0}{3}\begin{bmatrix}0 & -i & 0 & 0 & 0 & 1\\ i & 0 & 0 & 0 & 0 & -i\\ 0 & 0 & 0 & -1 & i & 0\\ 0 & 0 & -1 & 0 & i & 0\\ 0 & 0 & -i & -i & 0 & 0\\ 1 & i & 0 & 0 & 0 & 0\end{bmatrix}\begin{matrix}x\uparrow\\ y\uparrow\\ z\uparrow\\ x\downarrow\\ y\downarrow\\ z\downarrow\end{matrix}, \quad (2)$$

where the zone-center spin-orbit splitting is

$$\Delta_0=3i\frac{\hbar}{4m^2c^2}\langle|(\nabla V_0\times\mathbf{p})_z|y\rangle. \quad (3)$$

The valence band structure is obtained by calculating the eigenvalues of $\underline{H}_{\mathbf{k}\cdot\mathbf{p}}+\underline{H}_{\text{s.o.}}$. The valence-band structure of bulk Si, obtained in this way, is shown in Fig. (1a). Use of this Hamiltonian allows rapid and accurate evaluation of the band structure in the vicinity of the valence-band edge, where the strain effects are most prominent. The procedure for determining the eigenvalues of this Hamiltonian is sufficiently simple that the hole energy can be calculated quickly and precisely, during the Monte Carlo operation. The hole eigenstates, which are used in calculating the scattering matrix elements for the scattering rates, are determined by solving for the eigenvectors of $\underline{H}_{\mathbf{k}\cdot\mathbf{p}}+\underline{H}_{\text{s.o.}}$.

The effect of strain due to lattice mismatch is included in the band-structure calculation with the use of the valence-band deformation-potential theory. A strain perturbation Hamiltonian for diamond lattices in the $|x\rangle,|y\rangle,|z\rangle$ basis has been developed by Pikus and Bir.[3] In the presence of spin-orbit coupling, the strain perturbation matrix, like the $\mathbf{k}\cdot\mathbf{p}$ matrix, $\underline{H}_{\mathbf{k}\cdot\mathbf{p}}$, becomes a 6×6 block diagonal matrix, and is shown below:

$$\underline{H}_\varepsilon = \begin{bmatrix} \underline{H}'' & \underline{0}_{3\times 3} \\ \underline{0}_{3\times 3} & \underline{H}'' \end{bmatrix} \begin{matrix} x,y,z\uparrow \\ x,y,z\downarrow \end{matrix},$$

$$\underline{H}'' = \begin{bmatrix} l\varepsilon_{xx}+m(\varepsilon_{yy}+\varepsilon_{zz}) & n\varepsilon_{xy} & n\varepsilon_{zx} \\ n\varepsilon_{xy} & l\varepsilon_{yy}+m(\varepsilon_{zz}+\varepsilon_{xx}) & n\varepsilon_{yz} \\ n\varepsilon zx & n\varepsilon_{yz} & l\varepsilon_{zz}+m(\varepsilon_{xx}+\varepsilon_{yy}) \end{bmatrix} \begin{matrix} x \\ y \\ z \end{matrix}. \quad (4)$$

The ε_{ij} are elements of the strain tensor. The quantities l, m, and n are valence-band deformation potentials and are related to the more commonly used deformation potentials a, b, and d by.[3]

$$a = \frac{l+2m}{3},$$
$$b = \frac{l-m}{3}, \quad (5)$$
$$d = \frac{n}{\sqrt{3}}.$$

For systems of interest in the present work, the epitaxial semiconductor layer is biaxially strained in the plane of the substrate, by an amount $\varepsilon_\parallel$, and uniaxially strained in the perpendicular direction, by an amount $\varepsilon_\perp$. For a thick substrate, the in-plane strain of the layer is determined from the bulk lattice constants of the substrate material, a_S, and the layer material a_L:

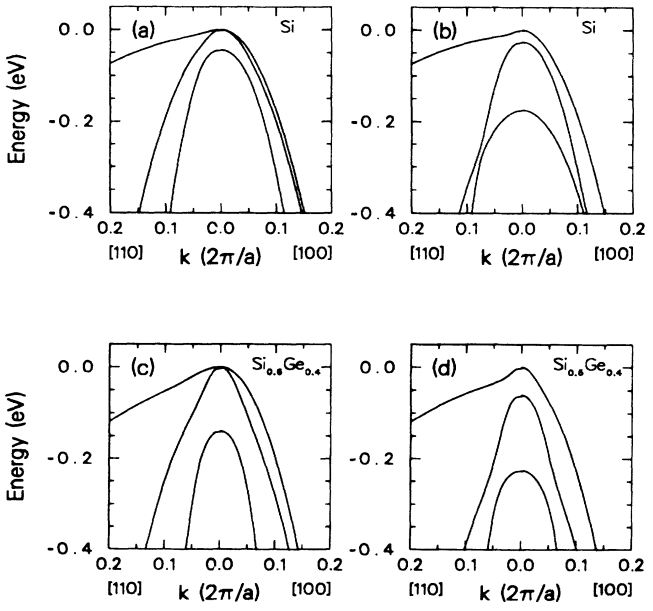

FIG. 1. Effect of strain and alloying on valence-band structure. (a) Bulk Si. (b) Biaxially compressed Si, $\varepsilon_{xx}=\varepsilon_{yy}=-0.0156$, $\varepsilon_{zz}=0.0119$. This is equal to the strain present in $Si_{0.6}Ge_{0.4}$ when grown epitaxially on Si(001). (c) Bulk (unstrained) $Si_{0.6}Ge_{0.4}$. (d) Pseudomorphic $Si_{0.6}Ge_{0.4}$/Si(001), $\varepsilon_{zz}=\varepsilon_{yy}=-0.0156$, $\varepsilon_{zz}=0.0119$. Material parameters used are given in Table I.

$$\varepsilon_\parallel = \frac{a_S}{a_L} - 1. \quad (6)$$

Since the layer is subjected to no stress in the perpendicular direction, the perpendicular strain $\varepsilon_\perp$ is simply proportional to $\varepsilon_\parallel$:

$$\varepsilon_\perp = -\frac{\varepsilon_\parallel}{\sigma}, \quad (7)$$

where the constant σ is known as Poisson's ratio and is dependent upon the crystallographic orientation of the substrate. For the case of growth on a (001) substrate, $\sigma = c_{11}/(2c_{12})$, where c_{11} and c_{12} are elastic stiffness tensor elements of the layer material. The effects of strain on the band structure are shown in Fig. 1.

Scattering rates for transitions from band n to band n' by mechanism m are calculated using Fermi's second golden rule:

$$W_{m;n,n'}(\mathbf{k}) = \frac{V_c}{(2\pi)^3}\frac{2\pi}{\hbar}\int d^3k' |M_{m;n,n'}(\mathbf{k},\mathbf{k}')|^2 \times \delta(E_n + \Delta E_m - E'_{n'}) = \int d\Omega' \frac{dW_{m;n,n'}(\mathbf{k},\mathbf{k}')}{d\Omega'}, \quad (8)$$

where $d^3k' = d\Omega' k'^2 dk'$. The domain of integration of the first integral is the entire Brillouin zone. The domain of the second integral is the constant final energy surface. M is the scattering matrix element, V_c is the crystal volume, and the density of final states is given by the δ function. The integrand $dW_{m;n,n'}(\mathbf{k},\mathbf{k}')/d\Omega'$ is referred to as a differential scattering rate, in analogy with a differential scattering cross section. The differential scattering rate is proportional to the postscattering probability distribution (Sec. III). Because of the complex warped nature of the valence-band constant energy surfaces, especially under strain, the above integration is carried out numerically in this work.

Alloy scattering is modeled after the work of Harrison and Hauser,[4] treating the $Si_{1-x}Ge_x$ system as a random alloy. The scattering potential is taken to be a spherically symmetric square well of depth U_0 and of spherical volume $\frac{4}{3}\pi r_0^3 = a_0^3/4$. This represents the effect of band structure fluctuations in the mixed alloy. The scattering matrix element is given by

$$\langle j'\mathbf{k}'|H|j\mathbf{k}\rangle = \delta_{\mathbf{k}'-\mathbf{k},\mathbf{q}} \frac{[Nx(1-x)]^{1/2}}{V_c} \times \frac{3\sin(qr_0)-3(qr_0)\cos(qr_0)}{(qr_0)^3} A^{j'j}, \quad (9)$$

where N is the number of primitive cells in the crystal, x is the germanium mole fraction, V_c is the crystal volume, q is the magnitude of the scattering wave vector, r_0 is the radius of the scattering center, and $A^{j'j}$ is the j',j element of the alloy scattering operator. The operator A is diagonal. To maintain consistency with the presentation of the phonon scattering operators, A may be written as a 3×3 matrix in the x,y,z basis

$$\underline{A}=\begin{bmatrix} U_0 & 0 & 0 \\ 0 & U_0 & 0 \\ 0 & 0 & U_0 \end{bmatrix}\begin{matrix} x \\ y \\ z \end{matrix}, \tag{10}$$

where U_0 is the alloy scattering potential.

Figures 2(a) and 2(b) show the alloy scattering rate as a function of hole energy. The data in these plots are given, setting $U_0=1.0$ eV. The actual scattering rate is obtained by multiplying the plotted value by $[U_0/(1\text{ eV})]^2$, since U_0 appears as a squared overall multiplicative factor in the scattering rate. Figure 2(a) shows a general increase in alloy scattering with increasing Ge content. However, for energies below 0.1 eV, it is seen that the alloy scattering rate is essentially independent of Ge content for Ge in the range of 20 to 40%. This is because the general trend of increase of the scattering rate as $x(1-x)$ is offset by the reduction in density of final states (i.e., reduction in effective mass) near the top of the heavy-hole band with increasing strain. Figure 2(b) shows alloy scattering for each of the nine types of intraband and interband transition considered for this and each of the other scattering mechanisms. These data

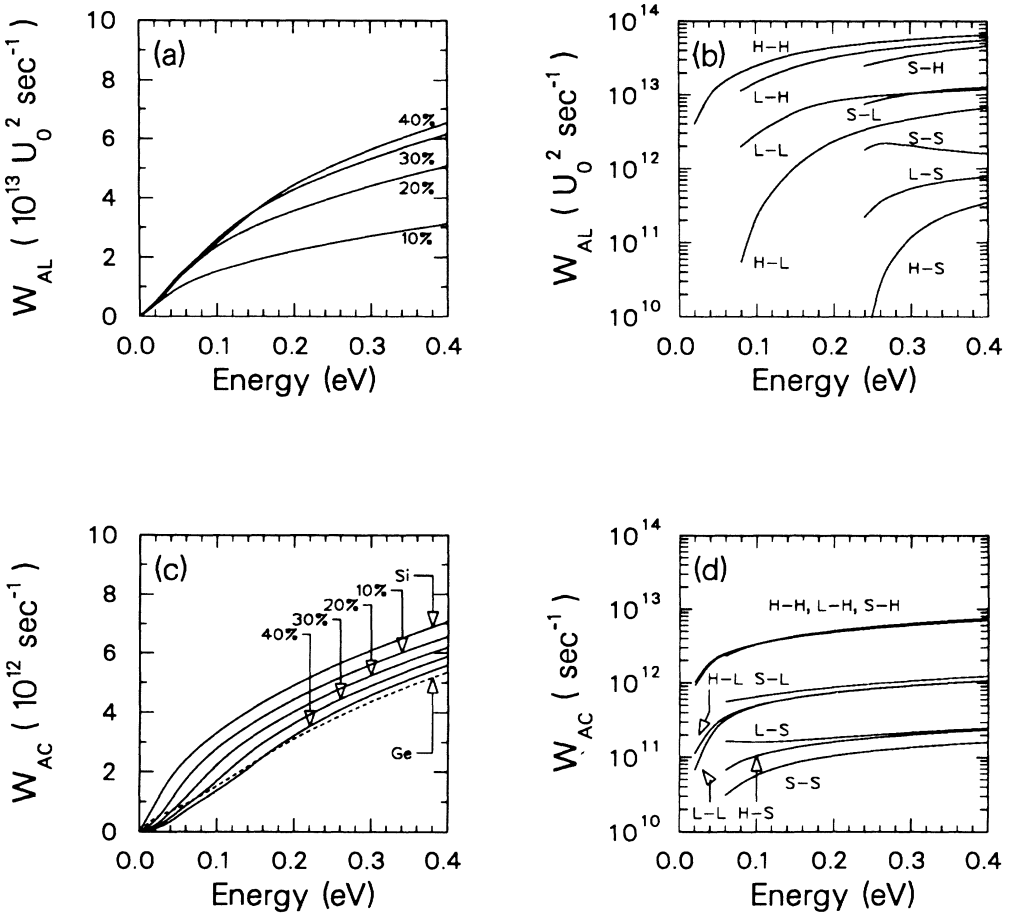

FIG. 2. Scattering rates for elastic scattering mechanisms. (a) Alloy scattering, heavy hole to heavy hole, [100] direction, in $Si_{0.9}Ge_{0.1}$ (10%); $Si_{0.8}Ge_{0.2}$ (20%); $Si_{0.7}Ge_{0.3}$ (30%); $Si_{0.6}Ge_{0.4}$ (40%). Scattering rate is plotted for $U_0=1.0$ eV. (b) Alloy scattering, intraband and interband, [100] direction, in $Si_{0.6}Ge_{0.4}$: *H-H* denotes heavy hole to heavy hole, *H-L* denotes heavy hole to light hole, *H-S* denotes heavy hole to split-off hole, *L-H* denotes light hole to heavy hole, *L-L* denotes light hole to light hole, *L-S* denotes light hole to split-off hole, *S-H* denotes split-off hole to heavy hole, *S-L* denotes split-off hole to light hole, *S-S* denotes split-off hole to split-off hole. Scattering rate is plotted for $U_0=1.0$ eV. (c) Acoustic-phonon scattering, heavy hole to heavy hole [100] direction, in Si; $Si_{0.9}Ge_{0.1}$ (10%); $Si_{0.8}Ge_{0.2}$ (20%); $Si_{0.7}Ge_{0.3}$ (30%); $Si_{0.6}Ge_{0.4}$ (40%); Ge (dotted line). (d) Acoustic-phonon scattering, intraband and interband, [100] direction, in Si: notation as in (b).

show that at high energies, away from the scattering thresholds, the order of magnitude of the scattering rate is determined by the final band, more than the initial band of the transition. Thus, for example, the scattering rate from the split-off band to the heavy-hole band at 0.4 eV is on the same order of magnitude as the heavy-hole intraband scattering rate. However, this does not mean that the frequency of scatterings from the split-off band to the heavy-hole band are as frequent as scatterings within the heavy-hole band. There will be, of course, more scatterings within the heavy-hole band simply because this band is much more heavily populated than the split-off band. Figure 2(b) shows that given a particle in a particular band, the probability of scattering to some final band is, to an order of magnitude, determined by the choice of final band, rather than the initial band. This is because the scattering rate strongly depends upon the density of final states. Other scattering mechanisms display the same behavior. Near threshold, however, the value of the scattering rate is strongly dependent upon both the initial and final band. In this case, the final wave vector is nearly zero because the top of each of the three valence bands is at the Brillouin-zone center. The scattering matrix element, which is dependent upon the initial wave vector as well as the final wave vector, will exert a strong influence upon the value of the scattering rate, for different choices of initial band.

Acoustic-phonon scattering is determined using the valence-band deformation-potential theory.[3,5,6] Using the equipartition theorem, the scattering matrix element for scattering by an acoustic phonon in branch l is given by

$$\langle j'\mathbf{k}'N'|H_l|j\mathbf{k}N\rangle = \delta_{\mathbf{k}'-\mathbf{k},\mathbf{q}}\, i \left[\frac{k_B T}{\rho V_c}\right]^{1/2} \sum_{\alpha,\beta=1}^{3} \frac{q_\alpha}{\omega_l(\mathbf{q})} e_\beta^l(\mathbf{q}) D_{\alpha\beta}^{j'j} , \quad (11)$$

where $k_B T$ is Boltzmann's constant times temperature, ρ is the mass density, V_c is the crystal volume, $\omega_l(\mathbf{q})$ is the phonon frequency in mode l, at wave vector $\mathbf{q}$, $e_\beta^l(\mathbf{q})$ is the βth component of the phonon polarization vector, and $D_{\alpha\beta}^{j'j}$ is the j',j element of the α,β deformation-potential operator. The above matrix element has a factor of $\sqrt{2}$ included to account for both emission and absorption, in one matrix element. The deformation-potential operator between valence-band states $j,j' = x,y,z$, is give by

$$D_{\alpha\beta}^{j'j} = \left\langle j' \left| \left[\frac{\hbar^2}{m} \frac{\partial^2}{\partial x_\alpha \partial x_\beta} + V_{\alpha\beta} \right] \right| j \right\rangle , \quad (12)$$

where $V_{\alpha\beta}$ is the rate of change of the lattice potential with strain:[3]

$$V_{\alpha\beta} = \frac{\partial V((1+\varepsilon)\mathbf{x})}{\partial \varepsilon_{\alpha\beta}} \bigg|_{\varepsilon=0} . \quad (13)$$

The operators $D_{\alpha\beta}$ are given as 3×3 matrices in the x,y,z basis:

$$\underline{D}_{xx} = \begin{bmatrix} l & 0 & 0 \\ 0 & m & 0 \\ 0 & 0 & m \end{bmatrix}, \quad \underline{D}_{yy} = \begin{bmatrix} m & 0 & 0 \\ 0 & l & 0 \\ 0 & 0 & m \end{bmatrix}, \underline{D}_{zz} = \begin{bmatrix} m & 0 & 0 \\ 0 & m & 0 \\ 0 & 0 & l \end{bmatrix} \begin{matrix} x \\ y \\ z \end{matrix} ,$$

$$\underline{D}_{xy} = \begin{bmatrix} 0 & \frac{n}{2} & 0 \\ \frac{n}{2} & 0 & 0 \\ 0 & 0 & 0 \end{bmatrix}, \quad \underline{D}_{yz} = \begin{bmatrix} 0 & 0 & 0 \\ 0 & 0 & \frac{n}{2} \\ 0 & \frac{n}{2} & 0 \end{bmatrix}, \quad \underline{D}_{zx} = \begin{bmatrix} 0 & 0 & \frac{n}{2} \\ 0 & 0 & 0 \\ \frac{n}{2} & 0 & 0 \end{bmatrix} \begin{matrix} x \\ y \\ z \end{matrix} , \quad (14)$$

and $\underline{D}_{xy} = \underline{D}_{yx}$, $\underline{D}_{yz} = \underline{D}_{zy}$, and $\underline{D}_{xz} = \underline{D}_{xz}$. The usual approach to hole–acoustic-phonon scattering[7,8] is formally equivalent to setting $\underline{D}_{xy}, \underline{D}_{yz}, \underline{D}_{zx} = \underline{0}_{3\times3}$ and replacing l and m with an averaged effective acoustic-phonon scattering deformation potential, Ξ_a, and replacing $\omega_l(\mathbf{q})/q$ with an averaged sound speed. In the present work we have not made this approximation and have retained the full anisotropic form of the deformation-potential operators $\underline{D}_{\alpha\beta}$. Figures 2(c) and 2(d) show the acoustic-phonon scattering rates as a function of hole energy. Figure 2(c) shows the heavy-hole intraband scattering rate for Si and Ge and for evenly spaced increments of Ge content in pseudomorphic $Si_{1-x}Ge_x$. The heavy-hole acoustic-phonon scattering rate steadily decreases for increasing Ge content in the pseudomorphic alloy and in the case of $Si_{0.6}Ge_{0.4}$, is comparable with that of bulk Ge. The data in Fig. 2(d) display the same dependence on choice of final band as described above, in the case of alloy scattering.

Nonpolar optical-phonon scattering is also treated as a deformation-potential scattering mechanism.[6] The scattering matrix element is given by

$$\langle j'\mathbf{k}'N'|H_l|j\mathbf{k}N\rangle = \delta_{\mathbf{k}'-\mathbf{k},\mathbf{q}} \delta_{N',N+1/2\mp1/2} \times \frac{1}{a_0} \left[\frac{3\hbar(n_0+\frac{1}{2}\mp\frac{1}{2})}{\rho\omega_0 V_c}\right]^{1/2} V_l^{j'j} , \quad (15)$$

where a_0 is the lattice constant, n_0 is the optical-phonon mean occupation number, ρ is the mass density, ω_0 is the zone-center optical-phonon frequency, V_c is the crystal

volume, and $V_l^{j'j}$ is the j',j element of the lth mode optical deformation-potential operator. The operators V_l are determined by the symmetry of the lattice,[6] and are given as 3×3 matrices in the x,y,z basis:

$$\underline{V}_x=\begin{bmatrix}0&0&0\\0&0&d_0\\0&d_0&0\end{bmatrix},\quad \underline{V}_y=\begin{bmatrix}0&0&d_0\\0&0&0\\d_0&0&0\end{bmatrix},$$
$$\underline{V}_z=\begin{bmatrix}0&d_0&0\\d_0&0&0\\0&0&0\end{bmatrix}\begin{matrix}x\\y\\z\end{matrix}, \tag{16}$$

where d_0 is the optical deformation potential. The optical-phonon spectrum is modeled as having a two mode behavior,[9] in which Si—Si bonds give rise to Si-like optical phonons and Ge—Ge bonds give rise to Ge-like optical phonons. The strength of each is taken to be proportional to the mole fraction of each respective alloy constituent.

Figure 3 shows the nonpolar optical-phonon scattering rate as a function of hole energy. The monotonic decrease in scattering rate with increase in Ge content in Fig. 3(a), is due to both a corresponding decrease in final density of states and a decrease in Si-Si optical-phonon population. Figure 3(b) gives the Si-Si nonpolar optical-phonon emission scattering rates for heavy holes in Si. The thresholds in these data correspond to the energy of 0.063 eV of the optical phonon for scattering to the heavy- and light-hole bands and to 0.107 eV, which is the sum of the spin-orbit splitting and the optical-phonon energy, for scattering to the split-off band. As with the elastic processes described above, the order of magnitude of the scattering rates is seen to depend primarily on the

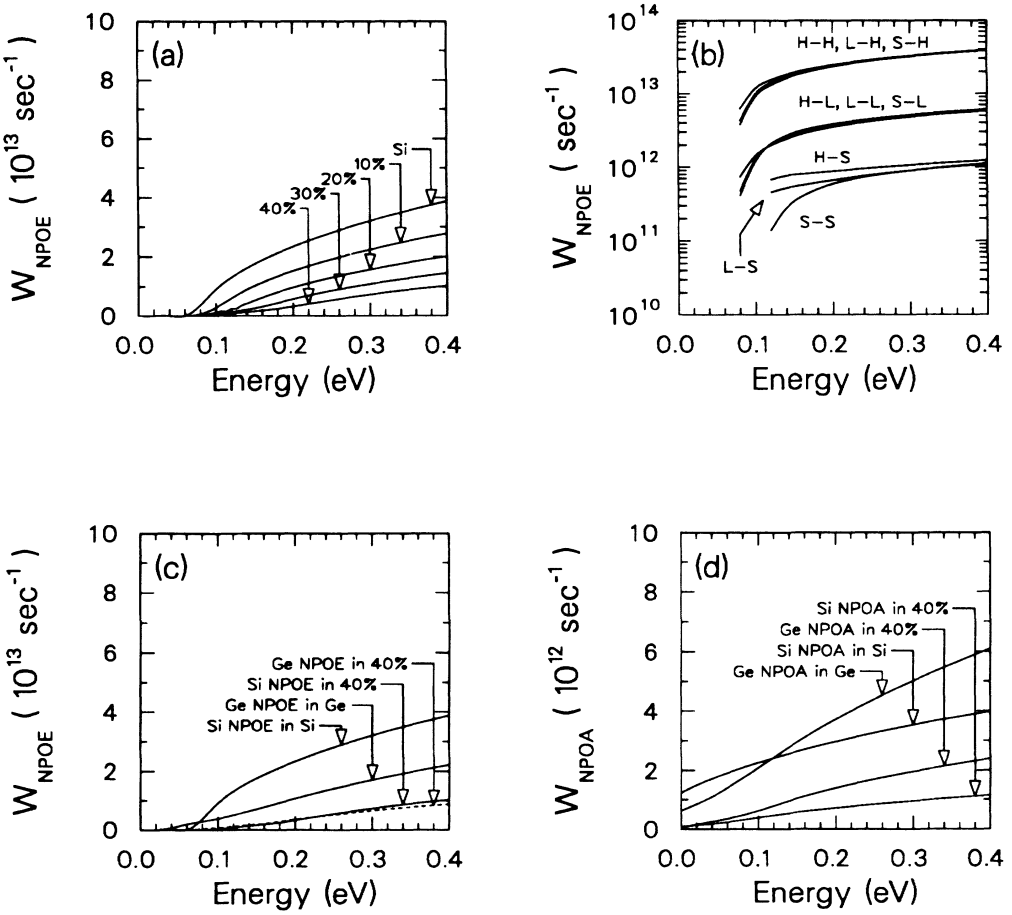

FIG. 3. Scattering rates for nonpolar optical-phonon scattering. (a) Si-Si optical-phonon emission scattering, heavy hole to heavy hole, [100] direction, in $Si_{0.9}Ge_{0.1}$ (10%); $Si_{0.8}Ge_{0.2}$ (20%); $Si_{0.7}Ge_{0.3}$ (30%); $Si_{0.6}Ge_{0.4}$ (40%). Monotonic decrease in scattering rate with increase in Ge content is due to both a corresponding decrease in final density of states and a decrease in Si-Si optical phonon population. (b) Si-Si optical-phonon emission scattering, intraband and interband, [100] direction, in Si: notation as in Fig. 2(b). (c) Si-Si and Ge-Ge optical-phonon emission scattering, heavy hole to heavy hole, [100] direction, in Si, Ge, and $Si_{0.6}Ge_{0.4}$ (40%). (d) Si-Si and Ge-Ge optical-phonon absorption scattering, heavy hole to heavy hole, [100] direction, in Si, Ge, and $Si_{0.6}Ge_{0.4}$ (40%).

choice of the final band, specifically, increasing with the density of final states. Figures 3(c) and 3(d) show the [100] heavy-hole intraband nonpolar optical-phonon scattering rates for emission and absorption, respectively. The energy of the Ge-Ge phonon is taken to be 37 meV and that of the Si-Si phonon to be 63 meV. The result of this is that the emission threshold is significantly lower for Ge-Ge phonon emission than for Si-Si emission, as seen in Fig. 3(c). Thus, the higher carrier mobility expected in a pseudomorphic material due to a reduced heavy-hole effective mass, compared to Si, will be tempered to some degree by the possibility of scattering by optical-phonon emission at lower energies than is the case in Si.

III. MONTE CARLO PROCEDURE

The Monte Carlo algorithm used in this work is an adaptation to anisotropic systems of the standard semiclassical charge-carrier transport algorithm such as was described and used by Fawcett, *et al.*[10] In the standard algorithm, as usually applied to electron transport, the band structure and scattering rates, involved in the simulation, are generally available in analytic form. This is in large part due to a dominantly *s*-like character of the cell periodic part of the electron Bloch function, near the conduction-band edge, in materials such as GaAs. In such cases this allows the use of simple spherical energy surfaces. This results in the ability to calculate the scattering rates as dependent upon the relative scattering angle, not both the initial and final trajectories separately. Furthermore, the portion of the conduction band, which is of primary interest in most cases, is comparatively well separated in energy from the other electronic bands of the material. This allows one to model the effects of other bands in particularly simple ways, such as the use of the band nonparabolicity factor $\alpha=1/E_g[(1-m^*/m_0)^2]$. The scattering rates usually have simple, analytical forms for materials with band structures described in this simple way. However, in the case of interest in the present work, the above approximations and techniques are no longer viable as means to describe the system. Owing to the anisotropy of the valence-band states (dominantly *p*-like), which is accentuated in the presence of strain, and the small energy separation between the heavy-hole, light-hole and split-off hole bands, completely numerical methods must be employed in determining both the band structure and the scattering rates. The band structure, itself, is calculated from the valence-band secular equation. The scattering rates depend upon the initial trajectories and are obtained by numerically integrating the differential scattering rates over the final constant energy surface. The differential scattering rates, themselves, depend upon both the initial and final trajectories, separately.

The transport simulation procedure is a sequence of particle free flights under an accelerating electric field followed by a scattering event, repeated until a stable value of drift velocity is obtained. In the present work, the duration of the free flight of the hole is determined in the usual way with the aid of a self-scattering mechanism.[11] However, the determination and resolution of the scattering event requires a detailed treatment. Three distinct scattering processes are used in the present work to model transport in unstrained Si and unstrained Ge, while six types of scattering process are required in the case of strained Si-Ge alloys. The three processes in unstrained Si and Ge are acoustic-phonon scattering, nonpolar optical-phonon emission, and nonpolar optical-phonon absorption. In the strained alloys, a distinction must be made between Ge-type optical phonons and Si-type optical phonons,[9] since the zone-center energy of the former is on the order of 37 meV and that of the latter, is on the order of 63 meV. The two types of phonons will be associated with distinctly different emission thresholds and resultant changes in hole energy during scattering. Also, the large energy difference will lead to a sizable difference in the mean occupation numbers of the two types of phonons. Thus, the two types of phonons cannot be merged into a single type with "average" properties. The alloy optical-phonon scatterings, therefore, result in four distinct types of scattering events: absorption and emission of each of the Si-type and the Ge-type phonon. The remaining two processes in alloy transport are acoustic-phonon scattering and random-alloy disorder scattering. Other phonon modes which may arise due to any special ordering effects in the material are not taken into account. It is expected that using the above modes is a reasonable approximation.

Transport in, and coupling between all three of the top valence bands (heavy hole, light hole, and split-off hole) have been accounted for in the present work. The split-off band in Si (zone-center spin-orbit splitting is equal to 0.044 eV) influence transport both by strongly coupling with the heavy- and light-hole bands and thus affecting the band structure and by carrying a certain amount of the current at high fields. These effects remain, although in a reduced degree, as the Ge content is increased in Si-Ge alloys. The inclusion of the split-off band, along with the heavy- and light-hole bands, leads to the consideration of three intraband and six interband modes of scattering for each type of scattering process, such as acoustic-phonon scattering. The resulting number of distinct types of scattering event (specified by the initial band, the final band, and the type of process), accounted for in the present work, totals 27 for unstrained Si and unstrained Ge and 54 for strained Si-Ge alloys. In an effort to reduce the complexity of the system, so that the effects of strain will be most clearly evident, ionized and neutral impurity scattering, as well as carrier-carrier scattering, have been omitted from this work. This corresponds to transport in an essentially pure material.

The scattering rate for each mechanism (e.g., heavy hole to light hole via acoustic-phonon scattering), is calculated on a mesh in reciprocal lattice space, which is designed to efficiently account for both the anisotropy and the symmetry of the system. On a particular mesh site, a calculated rate corresponds to the rate of scattering by the specified mechanism of a particle whose initial wave vector terminates on the mesh site's position in reciprocal space. In materials with cubic O_h symmetry, such as unstrained Si and unstrained Ge, the scattering

rates need only be calculated within an irreducible sector of the Brillouin zone such as that bounded by the high-symmetry Δ, Σ, and Λ axes, which correspond to $\frac{1}{48}$ of the full Brillouin zone. The scattering rate for a particle whose wave vector lies outside the irreducible sector may be obtained by transforming the particle's wave vector into the irreducible sector via one of the symmetry operations of the cubic O_h symmetry group, and then determining the rate from those calculated at specific wave vectors within this sector. Within each sector, specific radial axes or rays, which originate at the center of the Brillouin zone, are chosen. In the cubic system, for example, such rays might be the Δ ([001]) axis, the Σ ([101]) axis, and the Λ ([111]) axis. Along each ray, mesh points are chosen to correspond to equal steps in particle energy. These mesh points may therefore be viewed as determining concentric constant energy surfaces. The set of rays constitutes an angular mesh in reciprocal space, while the set of mesh points at each energy increment along each ray constitutes a radial mesh. The two meshes are used together to divide the reciprocal space into prism shaped elements, bounded on the corners by mesh points at which are calculated the scattering rates. At this point it is to be noted that the alternative of taking mesh points at equal intervals of wave-vector magnitude, rather than energy, was examined and found to be less suitable because of a characteristically large variation in a given scattering rate between different axes, for the same wave-vector magnitude. Use of the present mesh, in equal energy increments, allows a much more sparse angular mesh than would be required were equal wave-vector magnitude increments used in the radial direction.

The scattering rate associated with a particle after a simulated free flight is determined during Monte Carlo operation, by interpolation within the prism which contains the particle's wave vector. The interpolation is a weighted sum of the scattering rates on the six bounding mesh points. Each weighting factor is a product of two terms. The first term effects a linear interpolation in energy between the two triangular faces of the prism. The second term is formed by locating the position of the particle wave vector in the interior of the triangular prism face and dividing the prism face into three subtriangles $1',2',3'$. The three triangles are formed by drawing lines from the point at which the wave vector intersects the prism face to each of the three corners of the prism face. The weighting of a mesh point of the corner of the prism (e.g., corner 1) is then taken as the ratio of the area of the subtriangle opposite to this corner (e.g., subtriangle $1'$) to the total area of the prism face. This area ratio, multiplied by the factor of linear interpolation in energy, is used as a weighting factor for each of the six scattering rates on the bounding mesh points. The weighted scattering rates are then added to obtain the resulting scattering rate value for the given wave vector.

Strained materials, such as $Si_{1-x}Ge_x$/Si(001), exhibit tetragonal D_{4h}, not cubic O_h point-group symmetry. The reciprocal-lattice space irreducible sector of this system may be taken as $\frac{1}{16}$ of the Brillouin zone which is bounded by rays in the directions [001], [101], [111], [110], and [100]. In the present work this sector was further subdivided into three sections, bounded by [001], [101], and [111] (Sec. I), [111], [101], and [100] (Sec. II), and [100], [110], and [111] (Sec. III). These in turn were combined with the radial mesh in energy to subdivide the reciprocal space into prisms, as before.

Once all of the relevant scattering rates have been determined for a given particle, the acting scattering mechanism is chosen in the standard way with the aid of the self-scattering mechanism, as outlined in Ref. 10. This determines the change in particle energy and possibly band, as a result of scattering. The second stage of resolving a scattering event involves determining the orientation of the particle trajectory (i.e., wave vector) after scattering. For a given process (initial band, final band, scattering mechanism) and initial wave vector, the final particle trajectory is obtained with the aid of a postscattering state probability distribution $P(\cos\theta_s,\phi_s)$, which is proportional to the differential scattering rate $dW_{m;n,n'}(\mathbf{k},\mathbf{k}')/d\Omega'$:

$$P(\cos\theta_s,\phi_s) = \frac{dW_{m;n,n'}(\mathbf{k},\mathbf{k}')}{d\Omega'} \Big/ \max\left[\frac{dW_{m;n,n'}(\mathbf{k},\mathbf{k}')}{d\Omega'}\right], \quad (17)$$

where the maximum is over all final wave vectors $\mathbf{k}'$ which lie on the constant final energy surface. The explicit dependence of the probability distribution on the scattering azimuth ϕ_s must be retained since, generally, there is significant variation in $dW_{m;n,n'}(\mathbf{k},\mathbf{k}')/d\Omega'$ for constant θ_s. The scattering angles θ_s and ϕ_s are chosen by the standard von Neumann method,[10] using two random numbers to pick $\cos\theta_s$ and ϕ_s and a third to accept or reject the chosen $(\cos\theta_s,\phi_s)$ pair. After the scattering angles are chosen, the final trajectory is determined by operating on the final wave vector by the inverse of the symmetry operation which carried the initial wave vector into the irreducible sector of the Brillouin zone.

IV. RESULTS

The material parameters used in this work are given in Table I.[6,12–20] Material parameters for the alloy are not well documented in the literature over the wide range of composition used in this work. In the absence of such data, alloy material parameters are obtained by linear interpolation of the Si and Ge values. The elemental values are weighted by the mole fractions of the respective alloy constituents.

The effect of strain on the in-plane hole band structure of a $Si_{1-x}Ge_x$ layer is shown in Fig. 4(a). Shown are the band structures of Si and $Si_{0.6}Ge_{0.4}$/Si(001) (in-plane biaxial strain is equal to 1.56%). The effects of strain in splitting the heavy-hole–light-hole zone-center degeneracy as well as increasing the split-off band separation are evident. The effective mass at the top of the valence band is also lowered by the strain. Shown in Fig. 4(b) is the separation between the heavy-hole band edge, the light-hole band edge, and the split-off–hole band edge as a function of Ge content. The thresholds for inelastic nonpolar optical-phonon scattering follow the band edges at

a constant offset of the phonon energy with increasing Ge content. Therefore, an effect of strain and alloying is to suppress heavy-hole interband scattering by Si-Si optical-phonon emission as well as acoustic-phonon scattering, by pushing the respective interband transition thresholds to higher energies. Figure 4(c) shows the total density of states of the three valence bands in the strained alloy as well as in Si and Ge. These data were obtained by integration over the constant energy surface, as was done for calculating the scattering rates. The density of states decreases monotonically with increasing Ge content in the pseudomorphic alloy. The nonparabolicity is particularly evident in high Ge content alloys near the top of the valence band. At energies below 0.05 eV, $Si_{0.6}Ge_{04}$ has a lower density of states than Ge and remains close to the Ge density of states up to 0.1 eV. Both the increase in interband transition thresholds and the decrease in density of states with alloying and strain lead to a reduction in scattering rates and a corresponding increase in carrier mobility.

The hole-scattering rates are anisotropic, depending, at a given energy, upon the direction of flight. An example of this is shown in Fig. 5(a), in which the heavy-hole intraband acoustic-phonon scattering rate in $Si_{0.8}Ge_{0.2}$/Si(001) is shown as a function of energy for five different directions of flight: [100], [001], [111], [101], and [110]. It is to be noted that these are distinct directions in reciprocal space due to the tetragonal D_{4h} symmetry of the strained layer. Comparing the different scattering mechanisms, optical-phonon scattering is found to be dominant above 0.1 eV, well above its threshold. An example of this is shown in Fig. 5(b), where the heavy-hole intraband scattering rates in $Si_{0.8}Ge_{0.2}$/Si(001) are shown for [100] flight. Below 0.1 eV, optical-phonon scattering rates are comparable to acoustic-phonon scattering rates. The data of alloy scattering were calculated, assuming $U_0=0.2$ eV, which is the value used in the transport calculations of this work. Figure 5(c) shows the heavy-hole intraband and interband [100] scattering rates, summed over all types of scattering mechanisms, in $Si_{0.8}Ge_{0.2}$/Si(001). The intraband scattering is much larger than the others because of the larger density of final states in the heavy-hole band. Figure 5(d) shows the total heavy-hole [100] scattering rates for Si, Ge, 10–40 % Ge pseudomorphic alloy content. Si has the highest scattering rate, with the rate decreasing monotonically with Ge content. The scattering rates in $Si_{0.6}Ge_{0.4}$/Si(001) are less than the bulk Ge rates. The knee in the Si data at 0.063 eV is due to the threshold of Si-Si optical-phonon emission, which becomes the dominant scattering mechanism above this energy in Si. This feature is less present in the alloy data because of the presence of Ge-Ge optical phonons at a lower threshold (0.037 eV) and the reduction in population and thereby scattering strength of Si-Si optical phonons. The data shown in Fig. 5 correspond to scattering from states in the heavy-hole band only. The scattering rates from the light and split-off bands have similar features to the data plotted, with the largest rate being interband scattering to the heavy-hole band. These data have not been shown because they are quite similar to the plotted data and, furthermore, these transitions are less frequent due to the lower hole populations in these bands, thereby having less effect on the transport characteristics.

The postscattering state probability distributions, which are calculated over a mesh in both the initial and final wave vector, undergo a change of symmetry in the presence of strain. In Fig. 6 the postscattering state probability distributions of the acoustic-phonon scattering for a hole with incident energy of 10 meV, traveling in the [100] (in-plane) direction, are shown on the right, for Si, $Si_{0.8}Ge_{0.2}$/Si(001), and $Si_{0.6}Ge_{0.4}$/Si(001). The

TABLE I. Material parameters. Alloy parameters are obtained by linear interpolation: $P^{Si_{1-x}Ge_x}=(1-x)P^{Si}+xP^{Ge}$.

Material parameter	Symbol	Units	Si value	Ref.	Ge value	Ref.
Valence-band structure	L	(eV Å^2)	−25.51	12	−143.32	12
	M	(eV Å^2)	−15.17	12	−22.90	12
	N	(eV Å^2)	−38.10	12	−161.22	12
Spin-orbit splitting	Δ_0	(eV)	0.044	13	0.282	14
Deformation potential	a	(eV)	2.1	15	2.0	15
	b	(eV)	−1.5	15	−2.2	15
	d	(eV)	−3.4	15	−4.4	15
	d_0	(eV)	29.3	6	40.0	6
Lattice constant	a_0	(Å)	5.4309	16	5.6461	17
Elastic stiffness	c_{11}	(10^{11} dyn cm^{-2})	16.56	18	12.853	19
	c_{12}	(10^{11} dyn cm^{-2})	6.39	18	4.826	19
	c_{44}	(10^{11} dyn cm^{-2})	7.95	18	6.816	19
Mass density	ρ	(gm cm^{-3})	2.328	20	5.3243	20
Optical-phonon energy	$\hbar\omega_0$	(eV)	0.063	20	0.037	20

plots show the scattering rate dependence on the cosine of the scattering angle θ_s and azimuthal angle ϕ_s. On the left of these plots are shown the corresponding densities of states for the heavy-hole band at 10 meV. In case of Si, the postscattering state probability distribution has twelve maxima which correspond to the twelve maxima of the density of states in the [110] directions. As the strain is increased, the maxima of density of states shifts from the [110] directions to the [111] directions. Furthermore, the postscattering state distribution becomes twofold symmetric in azimuth, for the initial trajectory in the [100] (in-plane) direction, whereas in unstrained Si, it is fourfold symmetric. This also corresponds to a reduction in symmetry, under biaxial strain, about the direction of flight (x axis, [100]) of the density of states. The further structure in the polar angle dependence of the postscattering state distribution arises from the strain-induced effect on the scattering matrix element, which will be quantitatively different for each type of scattering mechanism.

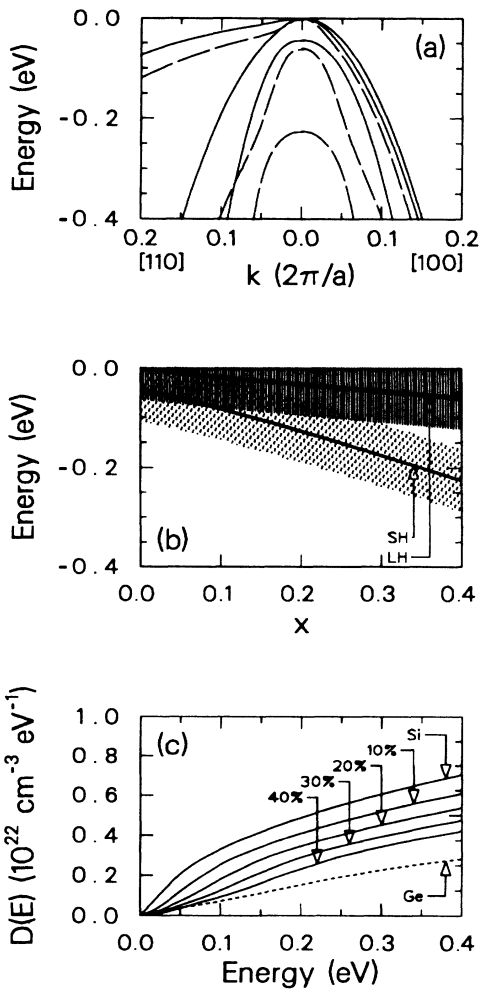

FIG. 4. Transition thresholds and densities of states. (a) Comparison of band structures of bulk Si (solid lines) and $Si_{0.6}Ge_{0.4}$/Si(001) (dashed lines). (b) Light-hole and split-off–hole bandedge shift with Ge content in $Si_{1-x}Ge_x$. The boundaries of the shaded areas correspond to the absorption and emission thresholds for Si-Si optical-phonon scattering. (c) Total density of states, $D(E)$, for Si; $Si_{0.9}Ge_{0.1}$ (10%); $Si_{0.8}Ge_{0.2}$ (20%); $Si_{0.7}Ge_{0.3}$ (30%); $Si_{0.6}Ge_{0.4}$ (40%); Ge (dotted line).

The velocity-field relations from the Monte Carlo calculations are shown in Figs. 7(a) and 8(a) for parallel (in-plane) and perpendicular transport, respectively. For comparison with measured velocities in Ge and Si, data from the literature,[21,22] are also shown. The corresponding chordal mobilities are shown in Figs. 7(b) and 8(b). These data are given relative to the chordal mobility of Si. The strained alloys show a monotonic increase of carrier velocity with Ge content. In the case of $Si_{0.6}Ge_{0.4}$/Si(001), the velocity is comparable to that of bulk Ge. A slightly higher velocity is found for in-plane, parallel transport than for perpendicular transport. It should be noted here that the alloy scattering potential strength, U_0, is now the only unknown parameter in our formalism. For the work presented so far, we have used an estimated value of $U_0=0.2$ eV. Although the alloy scattering is not the dominant scattering mode, it does have a quantitative effect on transport. In Fig. 9, the effect is shown of the alloy scattering potential U_0 on the velocity-field curves of $Si_{0.8}Ge_{0.2}$. Clearly the value of U_0 in the strained $Si_{1-x}Ge_x$ system needs to be measured experimentally in order to quantitatively give the change in carrier velocity with pseudomorphic alloying.

The hole population distributions are shown in Fig. 10 for in-plane transport. In Fig. 10(a), the hole population in Si is seen to broaden with increase in electric field. The carrier population becomes more dispersed with increased Ge content in the alloy, as shown in Figs. 10(b) and 10(c). The population dispersion is related to the effective carrier temperature, T_h, which can be calculated given the population distribution and density of states [Fig. 4(c)]. Assuming a nondegenerate material, the Fermi distribution function may be approximated by a Maxwellian distribution function. When this is multiplied by the density of states, the result is the population distribution for the given effective carrier temperature:

$$n(E)=\alpha e^{-(E/k_B T_h)} D(E) , \tag{18}$$

where n is the population distribution at energy E. α is an energy independent prefactor, depending upon the quasi-Fermi energy and the effective carrier temperature. $D(E)$ is the total density of states at energy E. When $n(E)$, calculated this way, is fitted to the simulated population distribution, as shown in Fig. 10, the effective carrier temperature may be determined. The results of such a fitting are shown in Fig. 11. It is found that the effective carrier temperature increases with Ge alloy content and with electric field. For low fields, around 1 kV/cm, the effective carrier temperature in $Si_{0.6}Ge_{0.4}$/Si(001) is slightly higher than in bulk Ge. At higher electric fields, however, the alloy effective carrier temperatures remain between that of Si and that of Ge. These data are given for a lattice temperature of 300 K (see Fig. 11).

An analysis of the relative numbers of each type of scattering event occurring during the Monte Carlo operation shows that for all alloy compositions ($0 \leq x \leq 0.4$) the most frequent type of scattering is heavy-hole intraband. These data are shown in Figs. 12(a) and 12(b), with $E = 5$ and 30 kV/cm, respectively. The carrier motion is in-plane [100]. The quantity plotted in these figures is the mean collision time, which is the total time of flight divided by the number of scatterings, of a given type, occurring in that period of time. The importance of inclusion of the split-off band in the analysis for high Si content materials is evident from these figures. These show that in pure Si and in $Si_{0.9}Ge_{0.1}$/Si(001), scatterings between the heavy-hole and split-off–hole bands are more frequent than intraband scatterings in the light-hole band. The situation reverses for higher Ge content alloys due to the associated increase in spin-orbit splitting. Generally, scatterings involving the split-off band become less frequent with increasing Ge content, as seen by the upward slopes of the *H-S L-S*, and *S-S* curves in Figs. 12(a) and 12(b). These data show why the valence-band transport cannot be modeled as transport in two decoupled bands (heavy and light holes). The heavy-hole–light-hole interband scattering is more frequent than the light-hole intraband scattering. This is because once a particle is in the light-hole band, the scattering rate to the heavy-hole band is much greater, due to the greater density of final states, than the scattering rate to

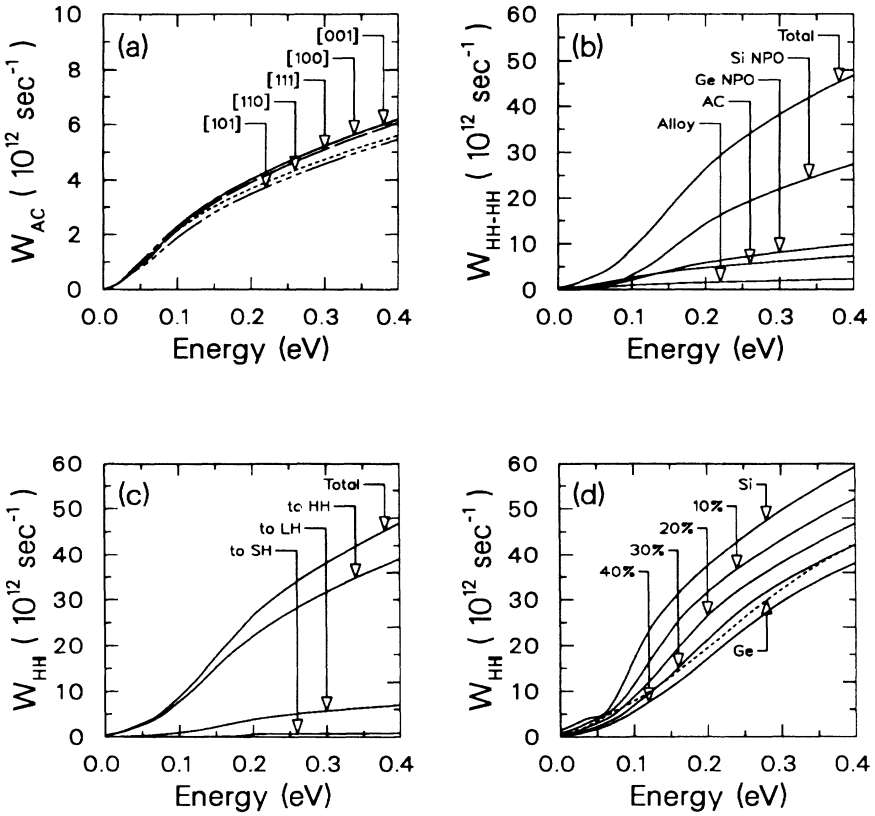

FIG. 5. Heavy-hole scattering rates. (a) Comparison of heavy-hole intraband acoustic-phonon scattering rates in $Si_{0.8}Ge_{0.2}$ for different directions of flight: [001], [100], [111], [110], and [101]. The scattering rates in the [001] and [100] directions overlap in this plot and are very nearly equal. (b) Heavy-hole [100] intraband scattering rates. Alloy denotes random-alloy scattering; $U_0 = 0.2$ eV. AC denotes acoustic-phonon scattering. Ge NPO denotes Ge-Ge nonpolar optical-phonon emission and absorption. Si NPO, Si-Si nonpolar optical-phonon emission and absorption. Total denotes sum of the four types. In the Monte Carlo operation, the inelastic processes of optical-phonon absorption and emission are treated as distinct. They have been plotted above as their sum just for simplicity. (c) Heavy-hole [100] intraband and interband scattering rates. HH, total scattering rate to the heavy hole band. LH, total scattering rate to the light hole band. SH, total scattering rate to the split-off hole band. Total denotes sum of these three types. (d) Total heavy-hole [100] scattering rates as a functions of alloy composition. Si; $Si_{0.9}Ge_{0.1}$ (10%); $Si_{0.8}Ge_{0.2}$ (20%); $Si_{0.7}Ge_{0.3}$ (30%); $Si_{0.6}Ge_{0.4}$ (40%); Ge (dotted line).

the light-hole band. In the case of Si and in $Si_{0.9}Ge_{0.1}$/Si(001), this statement may be extended to include the split-off band as well.

The most frequently occurring scattering mechanism is optical-phonon scattering, either Si-Si, for materials up to 30% Ge or Ge-Ge for $Si_{0.6}Ge_{0.4}$/Si(001). This is revealed by calculating the mean collision time per scattering mechanism, as shown in Figs. 12(c) and 12(d). The optical-phonon scattering curves include both emission and absorption, as do the acoustic-phonon scattering curves. The scattering frequency of Si-Si optical phonons becomes comparable with that of Ge-Ge optical phonons in the vicinity of 30% Ge. The fact that this equivalency occurs below 50%Ge is due to the Ge-Ge phonons having a lower energy (0.037 eV, compared to 0.067 eV for the Si-Si phonons) and therefore a higher phonon population than the Si-Si optical phonons. This increases the Ge-Ge optical-phonon scattering rate.

The results presented above are subject to four main assumptions or approximations. First of all, the material parameters used for the alloy are obtained by linear interpolation between the Si and Ge values. Sufficient experi-

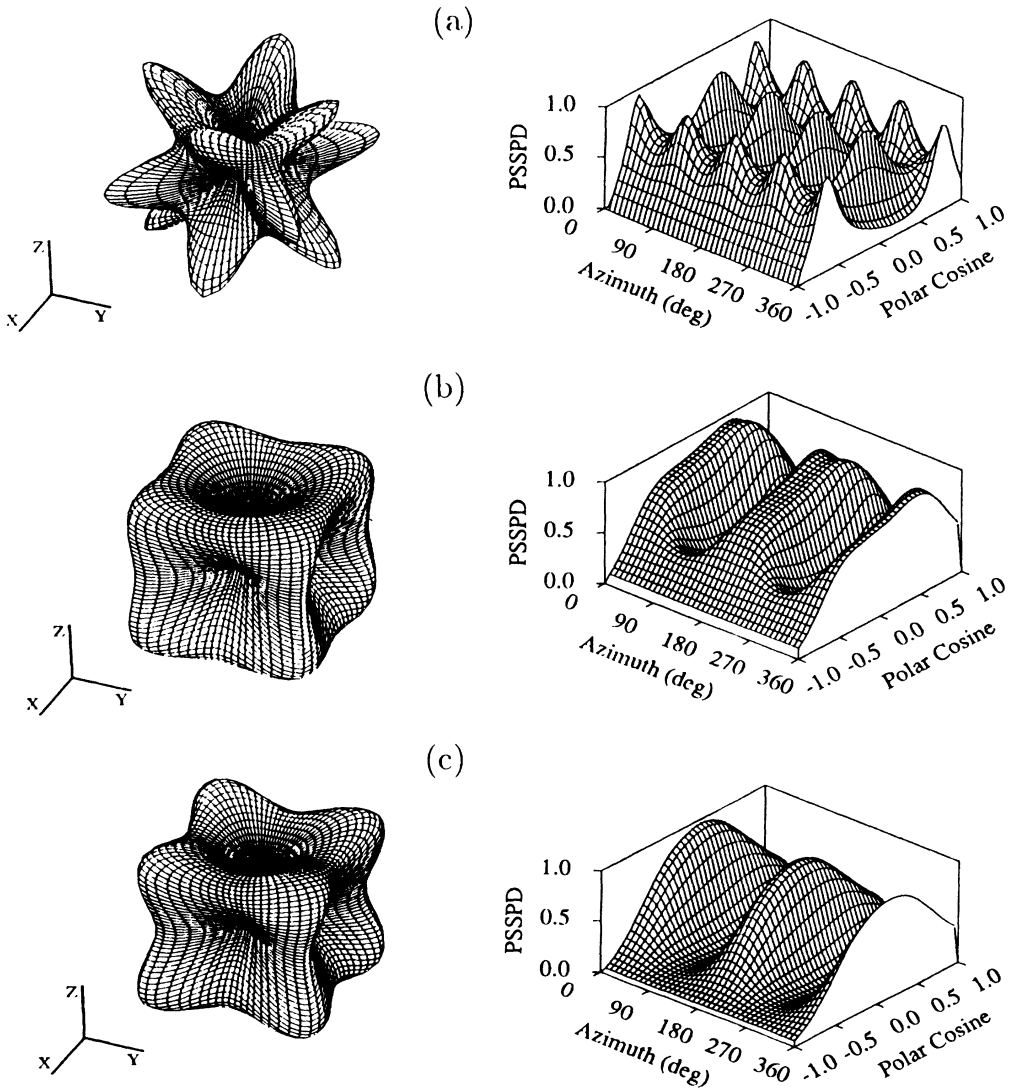

FIG. 6. Heavy-hole densities of states and heavy-hole [100] intraband acoustic-phonon postscattering state probability distributions, $P(\cos\theta_s\phi_s)$, at 0.01 eV. Densities of states are on the left in each part and the postscattering state distributions are on the right. (a) Si, $\varepsilon_{\parallel}=0$; (b) $Si_{0.8}Ge_{0.2}$/Si(001), $\varepsilon_{\parallel}=-0.0079$. (c) $Si_{0.6}Ge_{0.4}$/Si(001), $\varepsilon_{\parallel}=-0.0156$.

mental data in the literature have not been found to support the use of any other values. Secondly, a relatively simple picture is used for the alloy phonon spectra. The actual phonon spectra may be quite complicated and additional features may have to be accounted for. For example, there may be phonon localization due to the large difference between Si and Ge optical-phonon frequencies. Similarly, there may be mixed phonon modes. Some of these effects may depend upon the microcrystalline details of the grown structure. Clearly, if present, such effects must be accounted for and included in a formalism for hole transport. We believe that the dominant transport changes occur due to the electronic band-structure change, while phonon band-structure modifications will have secondary effects on the carrier transport. Thirdly, in modeling alloy scattering, we have assumed no alloy clustering. The presence of clustering may make alloy scattering relatively more important.[23] Also, we have assumed a value of alloy scattering potential of 0.2 eV. We have shown that the choice of the value of this parameter can be expected to have an observable effect on the car-

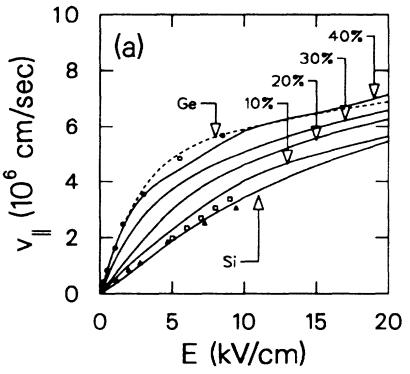

FIG. 7. Parallel (in-plane) transport characteristics. (a) Velocity-field relation for Si, $Si_{0.9}Ge_{0.1}$ (10%); $Si_{0.8}Ge_{0.2}$ (20%); $Si_{0.7}Ge_{0.3}$ (30%); $Si_{0.6}Ge_{0.4}$ (40%); Ge (dotted line). $U_0=0.2$ eV. Experimental data: circles, triangles (Ref. 21), and squares (Ref. 22). (b) Chordal mobility from data of (a), plotted relative to Si chordal mobility.

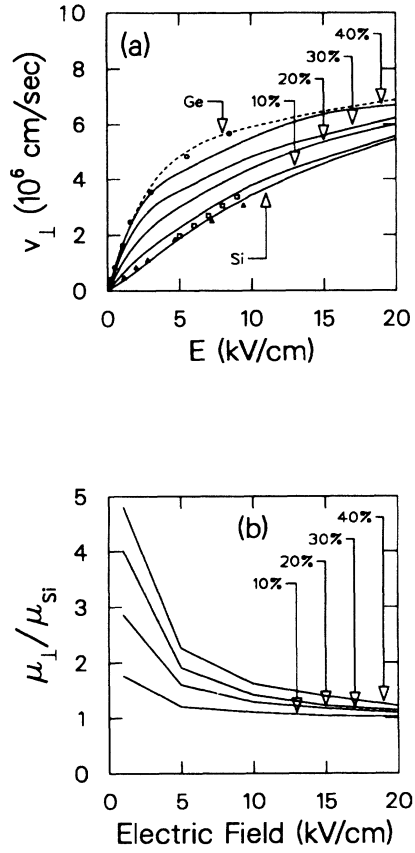

FIG. 8. Perpendicular transport characteristics. (a) Velocity-field relation for Si, $Si_{0.9}Ge_{0.1}$ (10%); $Si_{0.8}Ge_{0.2}$ (20%); $Si_{0.7}Ge_{0.3}$ (30%); $Si_{0.6}Ge_{0.4}$ (40%); Ge (dotted line). $U_0=0.2$ eV. Experimental data: circles, triangles (Ref. 21), and squares (Ref. 22). (b) Chordal mobility from data of (a), plotted relative to Si chordal mobility.

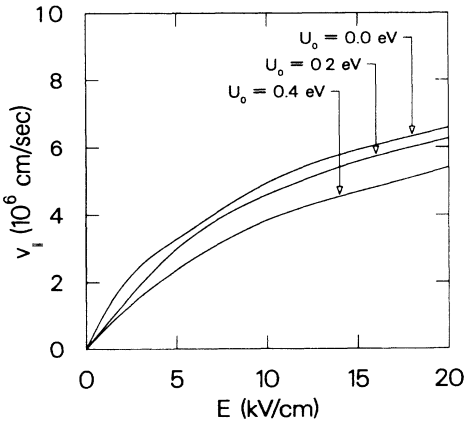

FIG. 9. Variation of velocity-field relation with alloy scattering potential U_0 in $Si_{0.8}Ge_{0.2}$. $U_0=0.2$ eV is used in the rest of this work.

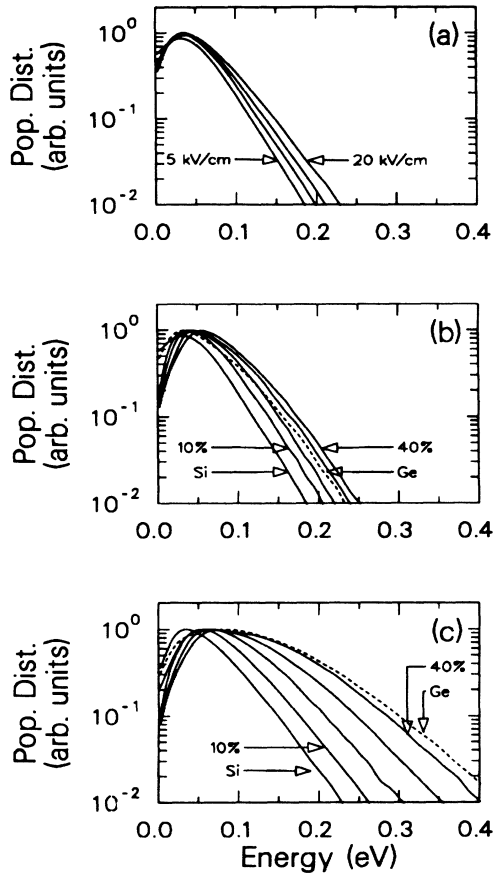

FIG. 10. Hole population distributions, for in-plane transport. (a) Population distribution in Si for $E=5$, 10, 15, and 20 kV/cm. (b) Population distribution at $E=5$ kV/cm in Si, $Si_{0.9}Ge_{0.1}$ (10%); $Si_{0.8}Ge_{0.2}$ (20%); $Si_{0.7}Ge_{0.3}$ (30%); $Si_{0.6}Ge_{0.4}$ (40%); Ge (dotted line). (c) Population distribution at $E=20$ kV/cm in Si, $Si_{0.9}Ge_{0.1}$ (10%); $Si_{0.8}Ge_{0.2}$ (20%); $Si_{0.7}Ge_{0.3}$ (30%); $Si_{0.6}Ge_{0.4}$ (40%); Ge (dotted line).

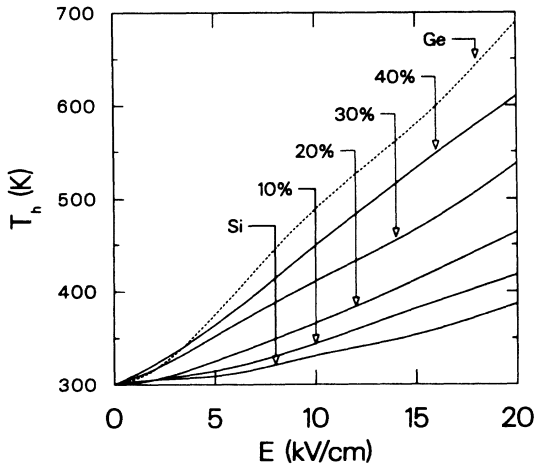

FIG. 11. Effective hole temperature at a lattice temperature $T=300$ K, for in-plane transport. Si, $Si_{0.9}Ge_{0.1}$ (10%); $Si_{0.8}Ge_{0.2}$ (20%); $Si_{0.7}Ge_{0.3}$ (30%); $Si_{0.6}Ge_{0.4}$ (40%); Ge (dotted line).

rier mobility. To our knowledge, however, this parameter has not been experimentally determined for the pseudomorphic system, to date. This data is required to improve our assumption of $U_0=0.2$ eV. Finally, we have neglected impurity and carrier-carrier scattering in our analysis of intrinsic and relatively pure materials. Applications of $Si_{1-x}Ge_x$ such as the base of a heterojunction bipolar transistor, however, make use of highly doped material. In such material, impurity scattering is expected to be important, leading to a different velocity-field characteristic than for intrinsic material.

V. CONCLUSION

An analysis of high-field hole transport properties due to lattice and alloy disorder scattering in $Si_{1-x}Ge_x$/Si(001) has been made by Monte Carlo simulation. Several aspects which make hole transport complex

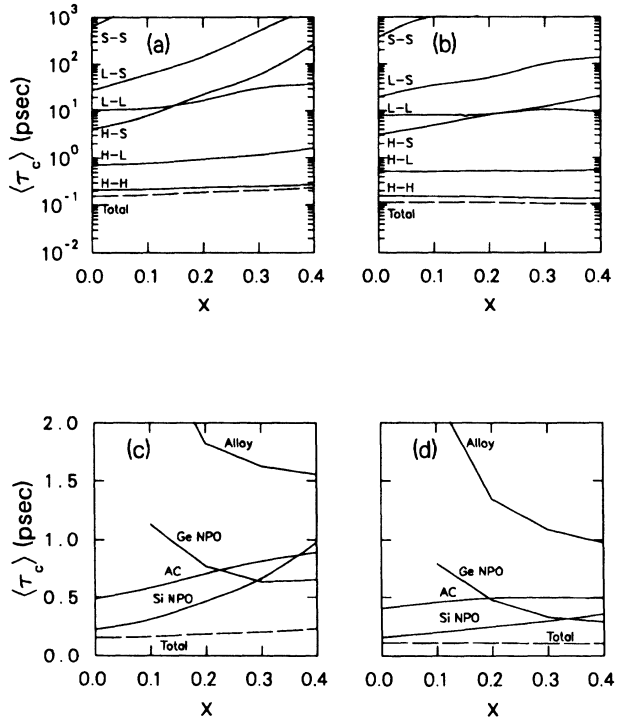

FIG. 12. Mean collision times. (a) Interband and intraband mean collision times for $E=5$ kV/cm, in-plane transport: *H-H* denotes heavy-hole intraband, *H-L* denotes heavy-hole–light-hole interband, *H-S* denotes heavy-hole–split-off–hole interband, *L-L* denotes light-hole intraband, *L-S* denotes light-hole–split-off–hole interband, *S-S* denotes split-off–hole intraband, total denotes sum of the six types. (b) Same as (a) for $E=20$ kV/cm. (c) Mean collision times by scattering process, $E=5$ kV/cm, in-plane transport: Alloy denotes random-alloy scattering; $U_0=0.2$ eV. AC denotes acoustic-phonon scattering. Ge NPO denotes Ge-Ge nonpolar optical-phonon emission and absorption. Si NPO=Si-Si nonpolar optical-phonon emission and absorption. Total denotes sum of the four types. (d) Same as (c) for $E=20$ kV/cm.

to model, have been taken into account. Included are the effects of interband coupling, anisotropic, nonparabolic energy surfaces, and the full operator form of the lattice scattering mechanisms.

A regular, monotonic increase in hole mobility and effective temperature is found with increasing Ge alloy content from 0 to 40% Ge. The hole transport properties in $Si_{0.6}Ge_{0.4}$/Si(001) are found to be closely similar to the hole transport properties in bulk Ge. The increase in hole mobility is due primarily to two strain related effects: (1) lifting of the zone-center heavy-hole–light-hole degeneracy and increased separation of the split-off–hole band, and (2) a reduction in the density of states, or equivalently, the effective mass of the carriers.

The results presented, however, are subject to a few qualifications. Nevertheless, we believe that these assumptions are justified, given the present state of knowledge about this material system. The aim of this paper is to present the realistic effects of strain on hole transport in the technologically important $Si_{1-x}Ge_x$/Si(001) material system. The analysis was carried out, retaining the most important features of both the valence bandstructure and hole scattering mechanisms. Further refinements to this model await accurate experimental determination of several of the properties of the pseudomorphic $Si_{1-x}Ge_x$/Si(001) system, most notably, characterization of alloy scattering.

ACKNOWLEDGMENTS

This work was supported by the U.S. Army Research Office (Grant No. DAAL03-87-K-0007), and by the U.S. Air Force (Grant No. F33615-87-C-1406). The authors also gratefully acknowledge support from the San Diego Supercomputer Center.

[1]G. Dresselhaus, A. F. Kip, and C. Kittel, Phys. Rev. **98**, 368 (1955).
[2]M. Tiersten, IBM J. Res. Dev. **5**, 122 (1961).
[3]G. E. Pikus and G. L. Bir, Fiz. Tver. Tela. (Leningrad) **1**, 1642 (1959) [Sov. Phys.—Solid State **1**, 1502 (1959)].
[4]J. W. Harrison and J. R. Hauser, Phys. Rev. B **13**, 5347 (1976).
[5]F. L. Madarasz and F. Szmulowicz, Phys. Rev. B **24**, 4611 (1981).
[6]F. Szmulowicz, Phys. Rev. B **28**, 5943 (1983).
[7]M. Costato, G. Gagliani, and L. Reggiani, Lett. Nuovo Cimento **4**, 171 (1972).
[8]E. M. Conwell and M. O. Vassell, Phys. Rev. **166**, 797 (1968).
[9]S. S. Mitra and N. E. Massa, *Handbook on Semiconductors*, edited by W. Paul (North-Holland, Amsterdam, 1982), Vol. 1, Chap. 3.
[10]W. Fawcett, A. D. Boardman, and S. Swain, J. Phys. Chem. Solids **31**, 1963 (1970).
[11]H. D. Rees, J. Phys. Chem. Solids **30**, 643 (1969).
[12]P. Lawaetz, Phys. Rev. B **4**, 3460 (1971).
[13]L. M. Roth, B. Lax, and S. Zwerdling, Phys. Rev. **114**, 90 (1959).
[14]S. H. Groves, C. R. Pidgeon, and J. Femleib, Phys. Rev. Lett. **17**, 643 (1966).
[15]J. D. Wiley, Solid State Commun. **8**, 1865 (1970).
[16]H. Kiendl, Naturforsch. **22a**, 79 (1967).
[17]S. M. Sze, *Physics of Semiconductor Devices* (Wiley, New York, 1981), Appendix F.
[18]H. J. McSkimin and P. Andreatch, J. Appl. Phys. **35**, 2161 (1964).
[19]H. J. McSkimin and P. Andreatch, J. Appl. Phys. **34**, 651 (1963).
[20]S. M. Sze, Ref. 17, Appendix H.
[21]E. J. Ryder, Phys. Rev. **90**, 766 (1953).
[22]A. Alberigi Quaranta, M. Martini, G. Ottaviani, G. Redaelli, and G. Zanarini, Solid State Electron. **11**, 685 (1968).
[23]W. P. Hong, A. Chin, N. Debbar, J. M. Hinckley, P. K. Bhattacharya, J. Singh, and R. Clarke, J. Vac. Sci. Technol. B **5**, 800 (1987).